Available online at www.sciencedirect.com

ScienceDirect

IFAC Papers Online CONFERENCE PAPER ARCHIVE

IFAC PapersOnLine 56-2 (2023) 5747–5752

Optimal Positioning of Snake Robots in Vortex Wakes using Extremum-Seeking Control

Amer Orucevic†, Mads Erlend Bøe Lysø†, Henrik Schmidt-Didlaukies, Kristin Ytterstad Pettersen, Jan Tommy Gravdahl

Centre for Autonomous Marine Operations and Systems (NTNU AMOS), Department of Engineering Cybernetics, Norwegian University of Science and Technology (NTNU), Trondheim, Norway (e-mail: {amer.orucevic, mads.e.b.lyso, henrik.schmidt, kristin.y.pettersen, jan.tommy.gravdahl}@ntnu.no)

Abstract: In this paper we explore the optimal positioning of an underwater snake robot (USR) for energy harvesting in the wake of a bluff body. The USR and fluid are simulated jointly using a coupled vortex particle-mesh method and multi-body system solver. The power dissipated in the damped joints of the robot is used as a proxy for the harvested energy. Furthermore, the effect of different damper coefficients on power dissipation is explored. An extremum-seeking control (ESC) scheme for nonlinear systems with time-varying steady-state solutions is employed to optimize the horizontal placement of the robot. The results show that the dissipated power does have a clear optimum. Moreover, the horizontal position of the USR under the ESC scheme is demonstrated to converge to a vicinity of the optimal position.

Keywords: Nonlinear and optimal marine system control, Energy Autonomy, Robotics technology, Autonomous robotic systems, Autonomous underwater vehicles.

1. INTRODUCTION

Our understanding of the oceans is crucial for meeting challenges such as food sufficiency, bio-diversity, renewable energy, transport, and access to minerals and other resources. To fully access the vast oceans we need efficient, autonomous marine robots. One promising approach is to use underwater snake robots (USRs), which are autonomous underwater vehicles (AUVs) consisting of several slim segments connected by joints, allowing them to move by undulating like an eel (Kelasidi et al. (2016)). The advantage of this design is that it can access narrow spaces and interact with its environment since the vehicle is also a robotic manipulator.

Power delivery remains a challenge for AUVs. Battery constraints limit their operational time, while tethers would limit their operational area and autonomy. Therefore, we want to pursue the idea of achieving energy autonomy for USRs by utilizing the motion induced in the joints when the USR operates in the wake of a bluff body (Bernier et al. (2019, 2018)). To this end, we investigate how the energy dissipated in the rotational dampers between the links changes as the distance to the bluff body is altered in a numerical high-fidelity simulation. Then an extremum-seeking controller is implemented to find the optimal distance to the bluff body and the results from the high-fidelity simulations are used to assess the performance of the ESC.

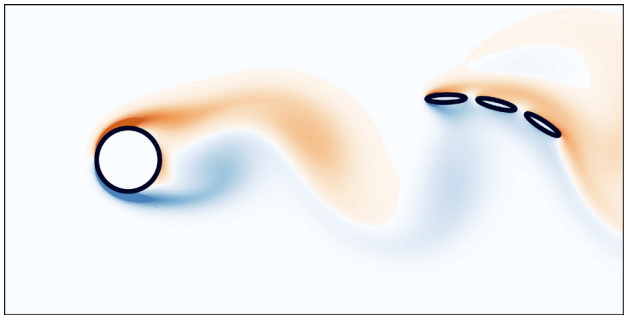

Fig. 1. Snapshot from the simulation of the swimmer in the vortex street behind a bluff body.

Energy harvesting for snake-like structures in vortex wakes behind bluff bodies has been studied with promising results. In Allen and Smits (2001), four piezoelectric membranes were placed in the wakes of two different bluff bodies. It was observed that the snake-like structures exhibited lock-in behavior to the bluff body shedding, which is a requirement for achieving optimal coupling. Lock-in behavior results in a resonance condition where the membrane has a minimal damping effect on the vortex street.

⋆ This result is part of a project that has received funding from the European Research Council (ERC) under the European Union's Horizon 2020 research and innovation programme, through the ERC Advanced Grant 101017697-CRÈME. The work is also supported by the Research Council of Norway through the Centres of Excellence funding scheme, project No. 223254 – NTNU AMOS.

† These authors contributed equally to this work

10.1016/j.ifacol.2023.10.535

The energy harvesting capabilities of an articulated three-link swimmer were investigated computationally in Bernier et al. (2019). The bodies are modelled as separated ellipses and connected through rotational dampers. Several different damping coefficients were studied, and the results indicate an optimal damping coefficient for harvesting energy. However, changing other parameters, such as the distance to the cylinder and the swimmer's size, might yield better harvesting efficiency.

In the field of model-free optimization, extremum-seeking control (ESC) has a long history. While the method can be traced back as far as 1922 to the work of Maurice Leblanc (Krstic and Wang, 1997), it has regained popularity in the last few decades after receiving more rigorous analytical treatment and systematization by e.g. Krstic and Wang (1997) and Nešić et al. (2010). However, for most of its history ESC has been limited to the optimization of systems that can be regulated to optimal constant set-points. The method as such has not been applicable to systems that exhibit periodic or generally time-varying steady-state behavior (e.g. stable limit-cycles). In Haring et al. (2013), a variation of ESC was developed for time-varying nonlinear systems with stable periodic steady-state behavior. However, the method requires that the period of the steady-state behavior is known a priori. Hazeleger et al. (2020) proposes a more general method, which can be used for nonlinear systems with unspecified time-varying steady-state solutions, as long as they are stable and bounded for each choice of system input.

In this paper we investigate the optimal positioning of a USR in a simulated vortex street. Specifically, we want to investigate whether the distance to the cylinder can be an important parameter to optimize the energy harvesting. We use the power dissipated in the damped joints of the robot as a proxy for the harvested energy, and we find that this has a clear optimum. Furthermore, we utilize the ESC method of Hazeleger et al. (2020) for nonlinear time-varying systems to maximize the energy dissipated in the joints of the robot by varying the distance between the USR and the bluff cylinder. The simulation of the snake-fluid system is performed using a vortex particle-mesh (VPM) method coupled with a multi-body system (MBS) solver based on an algorithm by Bernier et al. (2019).

The paper is organized as follows: In Section 2 the computational fluid dynamics (CFD) solver used in this paper is summarized and we present the methods used to investigate how the position of the USR affects the energy dissipated in the dampers. Then, an overview of the ESC-scheme applied to find the optimal position is presented. The simulation setups and results from the simulations are presented in Section 3. We demonstrate that there is an optimal horizontal position where the energy dissipated in the dampers of a multi-body swimmer is highest. Furthermore, it is shown that the ESC can be used to regulate the system towards this optimal distance. In Section 4 a conclusion is presented and future work is discussed.

2. METHODS

2.1 Coupled Solver

This section shortly summarizes the algorithm used to simulate a two-dimensional articulated swimmer in a complex fluid environment with fluid-structure interaction. The method is presented in Bernier et al. (2019) and relies on VPM techniques coupled with a MBS solver.

The VPM method solves the incompressible flow past deforming objects by using the velocity-vorticity formulation of the Navier-Stokes equations,

$$\frac{D\omega_f}{Dt} = (\omega_f \cdot \nabla)\boldsymbol{u}_f + \nu\nabla^2\omega_f, \tag{1a}$$

where D/Dt denotes the Lagrangian derivative, $\boldsymbol{u}_f$ is the velocity field, ν is the kinematic viscosity and ω_f is the vorticity field. The algorithm is summarized in Algorithm 1.

The first step in Algorithm 1 consists of recovering the velocity field from the vorticity field. Then, in the projection step, the fluid evolves as if the swimmer is not there. The resulting velocity field and position of particles, $\boldsymbol{u}_f^n$ and $\boldsymbol{x}$, are then used to predict the linear and angular momentum, $\boldsymbol{P}_{\text{proj}}$ and $\boldsymbol{I}_{\text{proj}}$, of the swimmer, respectively. The resulting forces and moments are given by $\boldsymbol{F}_{\text{proj}}$ and $\boldsymbol{M}_{\text{proj}}$, respectively. The dynamics of the swimmer are handled by the MBS solver and given by (4c) derived in Spong et al. (2006). The generalized coordinates of the swimmer are given by $\boldsymbol{q} = [q_1, ..., q_{n_{\boldsymbol{q}}}]^T$, where $[q_1, q_2]$ are the horizontal and vertical position of the first link, while q_3 is the absolute orientation of the first link. The relative angles between the links are given by $[q_4, ..., q_{n_{\boldsymbol{q}}}]$, an example-configuration is given in Fig. 2. The number of generalized coordinates is given by n_q. The generalized hydrodynamic forces and moments are obtained from the projection and penalization forces through a mapping $\mathcal{F}$, in our case the transposed Jacobian of the generalized coordinates, and given by $\boldsymbol{\tau}_{\text{hyd}}$, while the actuation forces are given by $\boldsymbol{\tau}_{\text{act}}$. The configuration is then translated into a characteristic function that describes the swimmer's shape χ_s through the mapping function $\mathcal{G}$. The velocity field of the structure is represented by $\boldsymbol{u}_s$, which is found in a similar fashion through the mapping function $\mathcal{H}$. The no-slip condition is then enforced by use of Brinkman penalization in (6a), resulting in the new velocity and vorticity fields, $\boldsymbol{u}_\lambda$ and ω_λ respectively. The forces and moments resulting from constraining the fluid, $\boldsymbol{F}_{\text{pen}}$ and $\boldsymbol{M}_{\text{pen}}$, are calculated in (6c) and (6d). Finally, the vorticity field is updated in (7a). Additionally, the time-step is constrained so that $\Delta t^n \leq \min\{C, h^2/2\nu, \Delta t^{\max}\}$ where $\Delta t^n = (t^{n+1} - t^n)$, C are the Lagrangian Courant-Friedrich-Levy conditions (LCFL) (Bernier et al. (2019)), and h is the uniform

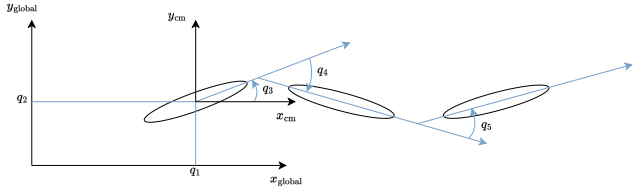

Fig. 2. Three-linked swimmer configuration.

Algorithm 1 Coupled Solver

While: $t^n \leq t^{\text{End}}$

1: Retrieve velocity field from vorticity field by solving the Poisson equation

$$\nabla^2 \boldsymbol{u}_f^n = -\nabla \times \omega_f^n. \tag{2}$$

2: Calculate projection forces and moments

$$\boldsymbol{P}_{\text{proj}}^{n+1} = \int_\Omega \rho_f \chi_s^n \boldsymbol{u}_f^n d\boldsymbol{x}, \qquad \boldsymbol{F}_{\text{proj}}^{n+1} = \frac{\boldsymbol{P}_{\text{proj}}^{n+1} - \boldsymbol{P}_{\text{proj}}^{n}}{\Delta t^n}, \tag{3a}$$

$$\boldsymbol{I}_{\text{proj}}^{n+1} = \int_\Omega \rho_f \chi_f^n (\boldsymbol{x} \times \boldsymbol{u}_f^n) d\boldsymbol{x}, \quad \boldsymbol{M}_{\text{proj}}^{n+1} = \frac{\boldsymbol{I}_{\text{proj}}^{n+1} - \boldsymbol{I}_{\text{proj}}^{n}}{\Delta t^n}. \tag{3b}$$

3: Time integration of MBS and update swimmer position and velocity

$$\boldsymbol{\tau}_{\text{hyd}}^{n+1} = \mathcal{F}(\boldsymbol{F}_{\text{proj}}^{n+1} + \boldsymbol{F}_{\text{pen}}^{n}, \boldsymbol{M}_{\text{proj}}^{n+1} + \boldsymbol{M}_{\text{pen}}^{n}), \tag{4a}$$

$$\boldsymbol{\tau}_{\text{act}}^{n+1} \rightarrow \text{provided by a control law}, \tag{4b}$$

$$D(\boldsymbol{q})\ddot{\boldsymbol{q}} + C(\boldsymbol{q}, \dot{\boldsymbol{q}}) = \boldsymbol{\tau}_{\text{act}}^{n+1} + \boldsymbol{\tau}_{\text{hyd}}^{n+1}. \tag{4c}$$

Compute $\boldsymbol{q}^{n+1}$ and $\dot{\boldsymbol{q}}^{n+1}$ for $t^{n+1} = t^n + \Delta t^n$

$$\chi_s^{n+1} = \mathcal{G}(\boldsymbol{q}^{n+1}), \quad \boldsymbol{u}_s^{n+1} = \mathcal{H}(\boldsymbol{q}^{n+1}, \dot{\boldsymbol{q}}^{n+1}). \tag{5a}$$

4: Penalization of vorticity field and calculation of penalization forces and moments

$$\boldsymbol{u}_\lambda^{n+1} = \frac{\boldsymbol{u}_f^n + \lambda \Delta t^n \chi_s^{n+1} \boldsymbol{u}_s^{n+1}}{1 + \lambda \Delta t^n \chi_s^{n+1}}, \tag{6a}$$

$$\omega_\lambda = \nabla \times \boldsymbol{u}_\lambda^{n+1}, \tag{6b}$$

$$\boldsymbol{F}_{\text{pen}}^{n+1} = \int_\Omega \lambda \rho_f \chi_s^{n+1} (\boldsymbol{u}_\lambda^{n+1} - \boldsymbol{u}_s^{n+1}) d\boldsymbol{x}, \tag{6c}$$

$$\boldsymbol{M}_{\text{pen}}^{n+1} = \int_\Omega \lambda \rho_f \chi_s^{n+1} \boldsymbol{x} \times (\boldsymbol{u}_\lambda^{n+1} - \boldsymbol{u}_s^{n+1}) d\boldsymbol{x}. \tag{6d}$$

5: Time integration of vorticity field

$$\frac{\partial \omega_\lambda}{\partial t} = \nu \nabla^2 \omega_\lambda - \nabla \cdot (\boldsymbol{u}_\lambda \omega_\lambda) \tag{7a}$$

$$\omega_f^{n+1} = \omega_\lambda^{n+1} \tag{7b}$$

End while.

spacing in the Cartesian discretization grid. The LCFL conditions may allow for time-steps that destabilize the MBS solver, therefore the time-step is constrained by a maximal time-step $\Delta t^{\max}$ which was found empirically.

2.2 Investigating the Optimal Positioning of USRs

As discussed in the Introduction, we want to investigate whether the distance to the cylinder can be an important parameter in optimizing the energy harvesting. In this section, we describe the method we will use to investigate whether there exists a well-defined optimal distance behind a bluff body with respect to the energy dissipated and whether the variation in dissipated energy is substantial as a function of distance.

A cylinder with diameter D_{cyl} and a planar USR with three links are submerged in a uniform free stream with a velocity U_f. The harvesting performance of the planar USR is assessed by considering the summed energy dissipated in the revolute dampers at each time step, given by

$$P_h(\dot{\mathbf{q}}) = \sum_{i=4}^{n_{\mathbf{q}}} K_{d,i} \dot{q}_i^2, \tag{8a}$$

$$\bar{P}_h^*(\{\dot{\mathbf{q}}(t^n)\}) = \frac{\sum_{t^n=t^s}^{t^{\text{End}-1}} \Delta t^n P_h(\dot{\mathbf{q}}(t^n))}{(t^{\text{End}} - t^s)\, \rho_f U_f^3 D_{\text{cyl}}}, \tag{8b}$$

where the damper-coefficients are given by $\{K_{d,i}\}_{i=4\ldots n_{\mathbf{q}}}$, P_h is the energy dissipated for a given generalized velocity, and $\bar{P}_h^*$ is the average dimensionless dissipated power over a solution of the discretized system. Additionally we define P^* as dimensionless power, and $t^* = tU_f/D_{\text{cyl}}$ as dimensionless time, where t is simulation time. The USR is prescribed to hold a constant position in the horizontal direction. The simulation is run several times at different distances from the bluff body, and the resulting $\bar{P}_h^*$ is compared. To avoid disturbances from the transient effects while the wake forms, the starting time for measurements, t^s, has to be selected sufficiently large.

As the steady-state behavior of a USR will be quasi-periodic, so will the dissipated power. However, we are interested in the average dissipated power. Thus, we find a smooth approximation of the average dissipated power as a function of distance. This approximation is obtained by placing the USR at a distance d_s from the bluff body. The dissipated energy is measured and fed through a low-pass (LP) filter with a cutoff frequency sufficiently low to filter out transients from the quasi-periodic oscillations of the USR when it operates in the wake. The distance is constant until the wake is fully formed and the LP-filter estimation has reached the quasi-constant equilibrium. The horizontal distance to the bluff body is then reduced at a constant rate a_d, sufficiently slow in comparison to the quasi-periodic behavior of the USR and the filter cutoff frequency. The filter acts as a very slowly-moving averaging operator, while the horizontal movement is slow enough to let the change in average power dissipation propagate through the filter. This allows us to assess whether P_h with the LP filter is a good evaluation of the performance while the USR is moving and if the optimal position coincides with the results from the grid-search where the USR held a constant position. Additionally, the results can be used as a ground truth when evaluating the performance of the ESC scheme.

2.3 Extremum-Seeking Control

In this section we present the ESC scheme which we will use to optimize the horizontal position of the robot. ESC is a method for model-free, online optimal control. Consider a non-specified time-invariant plant on the form

$$\dot{\mathbf{x}}(t) = \mathbf{f}(\mathbf{x}(t), \mathbf{u}(t), \mathbf{w}(t)), \ \mathbf{x}(0) = \mathbf{x}_0 \tag{9a}$$

$$\mathbf{y}(t) = \mathbf{g}(\mathbf{x}(t), \mathbf{u}(t)) \tag{9b}$$

where $\mathbf{x}(t)$ is the system state, $\mathbf{u}(t)$ is the input, $\mathbf{w}(t)$ is an unknown disturbance and $\mathbf{y}(t)$ is the output of the system. Define a cost function $c(\mathbf{y}(t))$. Assume that the plant is globally exponentially stable for any constant choice of $\mathbf{u}$, and that there exists an unknown function $\mathbf{l}(\mathbf{u})$ mapping a constant $\mathbf{u}$ to the corresponding equilibrium of the system. An objective function $F(\mathbf{u}) = c(\mathbf{g}(\mathbf{l}(\mathbf{u}), \mathbf{u}))$ can be associated to the cost, and $F(\mathbf{u})$ is not known explicitly. Then, an ESC scheme can be devised to drive $\mathbf{u}$ arbitrarily

close to its optimal value with respect to $F(\mathbf{u})$ (Ariyur and Krstić, 2003, pp.71 -73). ESC schemes are useful in a variety of scenarios due to its model-free nature. However, conventional ESC concerns itself only with plants whose steady-state behavior consists of convergence to an equilibrium point. In our case, a given horizontal position of the snake with respect to the cylinder will result in an oscillatory, periodic or quasi-periodic motion. We conjecture that by varying the horizontal position we can drive the plant to a *time-varying* steady-state behavior which is optimal with respect to power dissipation. In Hazeleger et al. (2020), an ESC scheme for nonlinear systems with arbitrary, time-varying steady-state behavior was introduced, and we will thus use this method to control the USR to its optimal position.

We now present a brief overview of the method introduced in Hazeleger et al. (2020) that is required to contextualize our application of the method. Please see Hazeleger et al. (2020) for further details of the method and proof of stability. A nonlinear system on the form (9) is considered. It is further assumed that the system is *globally uniformly exponentially convergent*, i.e., there is some uniformly exponentially stable trajectory denoted $\bar{\mathbf{x}}_{\mathbf{w}}(t,\mathbf{u})$ which is defined and bounded $\forall t \in \mathbb{R}$, for each constant choice of $\mathbf{u}$, and for all piece-wise continuous and bounded $\mathbf{w}(t)$.

Central to the method is the utilization of a *dynamic cost function*: A cost function $c(t) = Z(\mathbf{y}(t), \mathbf{u}(t))$ is processed through a filter subject to choice:

$$\dot{\mathbf{z}}(t) = \alpha_{\mathbf{z}}\mathbf{h}(\mathbf{z}(t), c(t)) \tag{10a}$$

$$l(t) = k(\mathbf{z}(t)) \tag{10b}$$

where $l(t)$ is referred to as the *dynamic cost function*.

We may denote the steady-state solution of the cost-function $\bar{c}_{\mathbf{w}}(t,\mathbf{u}) \triangleq Z(\bar{\mathbf{y}}_{\mathbf{w}}(t,\mathbf{u}),\mathbf{u})$, where $\bar{\mathbf{y}}_{\mathbf{w}}(t,\mathbf{u}) \triangleq \mathbf{g}(\bar{\mathbf{x}}_{\mathbf{w}}(t,\mathbf{u}),\mathbf{u},\mathbf{w}(t))$. While $\bar{c}_{\mathbf{w}}(t,\mathbf{u})$ is generally time-varying for any time-varying steady-state output, the filter acts so as to average $\bar{c}_{\mathbf{w}}(t,\mathbf{u})$ over time, leading to a slowly-varying dynamic cost which is quasi-constant even for time-varying input.

We then denote the solution of $\mathbf{z}$ under the input signal $\bar{c}_{\mathbf{w}}(t,\mathbf{u})$ as $\bar{\mathbf{z}}_{\mathbf{w}}(t,\mathbf{u})$. While the choice of $\mathbf{h}(\cdot)$ is left as a design parameter, the magnitude of $\alpha_{\mathbf{z}}$ can be chosen so as to make the dynamics of (10) arbitrarily slow. In the limit, the filter state becomes constant. We assume the existence of a twice continuously differentiable function $\bar{\mathbf{q}}_{\mathbf{w}}(\mathbf{u})$ defined as follows:

$$\bar{\mathbf{q}}_{\mathbf{w}}(\mathbf{u}) \triangleq \lim_{\alpha_{\mathbf{z}}\to\infty} \bar{\mathbf{z}}_{\mathbf{w}}(t,\mathbf{u}) \tag{11}$$

and refer to $\bar{\mathbf{q}}_{\mathbf{w}}(\mathbf{u})$ as the constant performance cost. We are now ready to define our objective function, and denote it as $F_{\mathbf{w}}(\mathbf{u}) \triangleq k(\bar{\mathbf{q}}_{\mathbf{w}}(\mathbf{u}))$. It is assumed that the dynamic cost function (10) is designed such that $F_{\mathbf{w}}(\mathbf{u})$ is twice continuously differentiable and has a unique minimum on $\mathbb{R}^{n_{\mathbf{u}}}$, the domain of system inputs. Furthermore, it is assumed that its directional derivative towards the optimum exhibits super-linear growth from the optimal point, and that its Hessian with respect to $\mathbf{u}$ is uniformly bounded, on $\mathbb{R}^{n_{\mathbf{u}}}$. The input for which $F_{\mathbf{w}}(\mathbf{u})$ reaches its minimum is referred to as $\mathbf{u}^*_{\mathbf{w}}$.

The Jacobian of the objective function is utilized to formulate an adaptation law for the current best approximation of $\mathbf{u}^*_{\mathbf{w}}$, denoted $\hat{\mathbf{u}}(t)$. As information about $F_{\mathbf{w}}$ is only available through observing $l(t)$, and as one in practice wants to choose $\alpha_{\mathbf{z}}$ low but nonzero, our knowledge of $F_{\mathbf{w}}$ is incomplete. Thus, we want to estimate both $F_{\mathbf{w}}$ and its Jacobian with respect to $\hat{\mathbf{u}}(t)$. In order to get information about the Jacobian of $F_{\mathbf{w}}$, we choose our input as $\mathbf{u}(t) = \hat{\mathbf{u}}(t) + \alpha_{\boldsymbol{\omega}}\boldsymbol{\omega}(t)$, where $\boldsymbol{\omega}(t) = \text{vec}\left(\{\omega_i(t)\}_{i\in 1\dots n_{\mathbf{u}}}\right)$ is a periodic signal designed to persistently excite the system.

A model is formulated to describe the behavior of the series-connected system from the nominal input, $\hat{\mathbf{u}}(t)$, to the filter output $l(t)$, in such a way that the state of the model becomes $\mathbf{m}(t) \triangleq \left[F_{\mathbf{w}}(\hat{\mathbf{u}}(t)), \alpha_{\boldsymbol{\omega}}\frac{\mathrm{d}}{\mathrm{d}\mathbf{u}}F_{\mathbf{w}}(\hat{\mathbf{u}}(t))^\top\right]^\top$. A least-squares observer is employed in order to produce an estimate $\hat{\mathbf{m}}(t)$, thereby also producing an estimate of the Jacobian of $F_{\mathbf{w}}$, denoted $\frac{\mathrm{d}}{\mathrm{d}\mathbf{u}}\hat{F}_{\mathbf{w}}(\hat{\mathbf{u}}(t))$.

Finally, an adaptive law can be formulated for $\hat{\mathbf{u}}(t)$:

$$\dot{\hat{\mathbf{u}}}(t) = -\lambda_{\mathbf{u}}\frac{\eta_{\mathbf{u}}\mathbf{D}\hat{\mathbf{m}}(t)}{\eta_{\mathbf{u}} + \lambda_{\mathbf{u}}\|\mathbf{D}\hat{\mathbf{m}}(t)\|} \tag{12}$$

where $\lambda_{\mathbf{u}}$, $\eta_{\mathbf{u}}$ are tuning parameters, and $\mathbf{D} = [\mathbf{0}_{n_{\mathbf{u}}\times 1}\ \mathbf{I}_{n_{\mathbf{u}}}]$. Under certain assumptions, which are given in Theorem 14 and Lemma 17 in Hazeleger et al. (2020), the system under the ESC scheme is semi-globally practically asymptotically stable, and $\lim_{t\to\infty}\|\hat{\mathbf{u}}(t) - \mathbf{u}^*\|$ has an upper bound dependent on controller parameters and the bound of the disturbance $\mathbf{w}(t)$.

2.4 Extremum-Seeking Control for the Snake-Fluid System

We now describe how we apply ESC to address the problem of maximal energy dissipation in damped joints, which we use as a proxy for maximal energy harvesting. Firstly, consider the USR rigid body system as formulated in (4c), where the horizontal position of the first link is directly prescribed by $u(t)$. We now define as our output $\mathbf{y}(t) = \dot{\mathbf{q}}(t)$. Then, we simply define the cost function as the negated sum of energy dissipated in the revolute joints of the robot, i.e. $c(\mathbf{y}(t)) = -P_h(\mathbf{y}(t))$, with $P_h(\cdot)$ defined as in (8a). Except from the prescribed, slowly-varying motion of the horizontal position of the first link, the USR is completely unactuated. Thus, the vast majority of the energy dissipated in the joint come from external disturbances on the system. The USR is affected by the forces from the fluid on each link. However, the dynamics of the fluid are too complex to be captured in closed-form, and the forces on the snake from the fluid are therefore included in the control scheme as an unknown, time-varying disturbance $\mathbf{w}(t)$. We are interested in maximizing the power dissipated in the USR, but the time-varying nature of the steady-state behavior at any given position means that the dissipated energy will also fluctuate greatly. The dynamic cost function described in (10), however, allows us to consider an averaged dissipated power which converges to a quasi-constant steady-state behavior for a constant u, and which we wish to optimize.

3. RESULTS

3.1 Simulation Setup

This section presents the parameters used during the simulations presented in this paper. The Reynolds number

is selected as $Re = 100$ for all simulations with a computational domain size given by $[0, 1.0] \times [0.0, 0.5]$ with a discretization grid resolution of $[1024, 512]$. The remaining parameters used in the simulations are given in Table 1. The parameter $\hat{\mathbf{H}} : \mathbb{R} \times \mathbb{R}^{n_\mathbf{u}} \to \mathbb{R}^{n_\mathbf{u} \times n_\mathbf{u}}$ is a function, here chosen constant, which factors into estimation of higher-order terms of $F_\mathbf{w}(\mathbf{u}(t))$ and is considered a controller design choice, see Hazeleger et al. (2020) for details. The swimmer dimensions are illustrated in Fig. 3, where the length and width from the center are given by a and b, respectively. The length from the tip of the ellipse to the rotational joint is given by c. A circular rigid body is positioned in front of the swimmer to act as a 2-dimensional bluff body and generate the vortex street. The horizontal and vertical positions of the cylinder centre mass are given by $[x^{\text{cm}}_{\text{cyl}}, y^{\text{cm}}_{\text{cyl}}]^\top$. See Fig. 1 for a snapshot of the simulation of the swimmer in the vortex street.

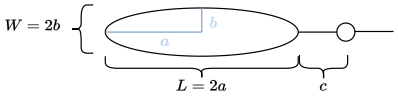

Fig. 3. Link and joint configuration.

3.2 Optimal Positioning

This section presents the results from the grid search of the average steady-state dissipated power as a function of the constant distance d_s. The distances used in the simulation are $[1.5, 1.75, 2.0, 2.25, 2.5, 2.75, 3.0] \times D_{\text{cyl}}$. We also present the results of a smooth approximation of the average steady-state dissipated power as a function of distance. This smooth approximation was rendered through a low-pass-filtering of the dissipated power resulting from a constant-velocity swipe of horizontal position, as described in Section 2.2. The resulting dissipated energy from the grid search with $[t^s, t^{\text{End}-1}] = [20s, 30s]$ and the smooth approximation are shown in the left and right subplots of Fig. 4, respectively.

The results from the grid search indicate that there is an optimal position that can be utilized. As can be seen in the left plot of Fig. 4, the optimal position is acquired at $d_s = 2.25 \times D_{\text{cyl}}$ for all configurations except $K_d = 0.005$, which has a optimal position at $d_s = 2.5 \times D_{\text{cyl}}$. The results indicate that the maximal dissipation rate increases with higher K_d up to $K_d = 0.01$. For $K_d = 0.0125$ the maximal dissipation rate is the same as that for $K_d = 0.01$, while the maximal dissipation rate is lower for $K_d = 0.0150$. However, we suspect this is a result of the grid being too coarse and that a finer grid would reveal that the optimal position varies continuously as a function of K_d, and is located between $d_s = [2.0, 2.75] \times D_{\text{cyl}}$ for the depicted choices of K_d. This also implies that the exact maximal value might not be captured in the grid search. We expect that a higher damper stiffness would lead to a higher $\bar{P}^*_h$. The optimal distance is slightly different for the grid search and the continuous approximation in Fig. 4, which may also be a result of the grid resolution or a result of the constant forward motion that induces some additional energy into the system.

The smooth approximation of average steady-state power dissipation further indicates that there are no local optima

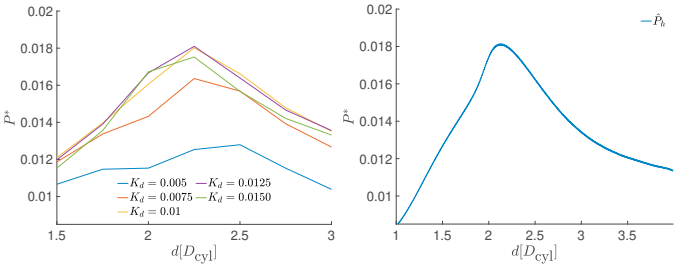

Fig. 4. Plots of the average dissipated power $\bar{P}^*_h$ for different damper coefficients K_d (left) and plot of the estimated average dissipated power from a low-pass filter as a function of the distance (right).

close to the global optimum on the interval considered. This lack of local peaks indicates that the distance may be well-suited for gradient-based optimization schemes, which will often struggle with local optima. However, one should also note that the slope seems to flatten out for greater distances from the cylinder, which may lead to slow convergence in these areas.

3.3 Extremum-Seeking Control

We now present the simulation results using the ESC scheme presented in Section 2.3 to maximize the energy dissipated in the joints of the USR through varying its horizontal distance behind a vortex-shedding bluff body. In Fig. 5, we see the resulting horizontal position and the corresponding dissipated power in the USR found by the ESC scheme. To initialize the system, the position is first held constant until a constant steady-state is reached in the filtered dissipated power, before the system is subjected to the ESC scheme.

The ESC scheme is seen in Fig. 5 to move fairly slowly at first, before picking up speed right before $t^* = 2000$ and converging shortly after. As is seen in Fig. 5, the horizontal position converges to an oscillatory behavior around the optimal distance $d_{s,\text{opt}}$ as obtained from the approximation depicted in Fig. 4. The flat slope of the dissipated power in the neighborhood around $d_s = 4.0$ in Fig. 4 helps explain the slow convergence towards the optimum when the position is in this interval. This demonstrates that the ESC scheme is capable of converging to the correct neighborhood, even when moving through difficult areas where $\|\frac{\text{d}}{\text{d}\mathbf{u}} F_\mathbf{w}(\mathbf{u})\|$ is small.

Fig. 5 shows that the dissipated power actually peaks before the ESC scheme converges, and that the peaks in the steady-state response are slightly above the maximum power $P_{h,\max}$ as obtained from the approximation depicted in Fig. 4. This may first seem counter-intuitive, but has a plausible explanation. The prescribed motion dictated by the ESC scheme also introduces kinetic energy, which propagates through the system and shows up as increased dissipated energy in the joints. While the added energy is small for slow movements, the increased rate of convergence before $t^* = 2000$, and the resulting increased change in input, likely results in more energy introduced through the prescribed motion for a short time interval. Nonetheless, as can be seen, the estimate of the gradient is not disturbed by this in a way that impedes the convergence of the scheme. We also observe that the oscillation in position

Table 1. Simulation parameters

U_f	D_{cyl}	a	b	c	ρ_f	ρ_s	C	$\Delta t^{\max}$	$x_{\text{cyl}}^{\text{cm}}$	$y_{\text{cyl}}^{\text{cm}}$
0.2	0.1	$0.3125D_{\text{cyl}}$	$0.2a$	$0.1D_{\text{cyl}}$	997	997	0.02	0.001	0.2	0.25
σ_r	$\mathbf{Q}_0$	$\hat{F}_{\mathbf{w},0}$	$\frac{\mathrm{d}}{\mathrm{d}\mathbf{u}}\hat{F}_{\mathbf{w},0}$	$\eta_{\mathbf{m}}$	$\eta_{\boldsymbol{\omega}}$	$\eta_{\mathbf{u}}$	$\lambda_{\mathbf{u}}$	$\alpha_{\boldsymbol{\omega}}$	$\hat{\mathbf{u}}_0$	$\hat{\mathbf{H}}$
0.1	$\begin{bmatrix}1.0 & 0\\ 0 & 1.67\end{bmatrix}$	0	10^{-4}	0.8	0.1	0.3	20.5	0.03	0.7	1.0

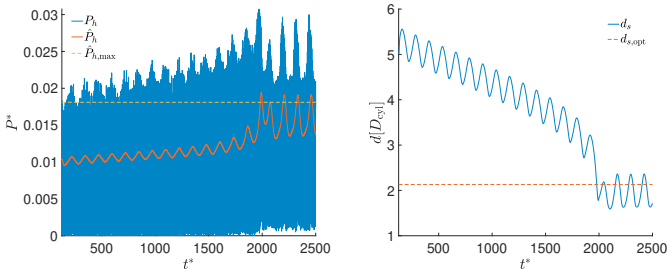

Fig. 5. Plots of the dissipated power and low-pass filtered dissipated power of the snake (left) and the prescribed horizontal position (right) under ESC.

towards the end of the simulation is not symmetric around the optimal position. This might be in part due to the scheme not having fully converged, and the small slope close to the optimum slowing down further convergence towards the actual steady-state behavior. This is supported by the slight upward trend that can be observed during the last oscillations in the position seen in Fig. 5.

It should be noted that there is a gap between even high-fidelity simulations and reality. However, we conjecture that the model-free nature of the ESC method makes the results resilient to minor simulation inaccuracies so long as the qualitative behavior of the system is captured.

4. CONCLUSIONS AND FUTURE WORK

In this paper, the optimal horizontal positioning of a USR in the vortex street of a bluff body with respect to power dissipation was investigated through high-fidelity simulations. It was found through a grid search that such an optimal position did indeed exist, and a smooth approximation of the dissipated power as a function of distance further indicated that no local optima exist in the close vicinity of the global optimum on the interval considered, for the bluff body in question. This supports that energy autonomy of USRs can be achieved by utilizing the motion induced when the USR operates in the wake of a bluff body, which was the motivation for our research.

Furthermore, an ESC scheme for nonlinear systems with time-varying steady-state solutions was employed to optimize over the distance from the bluff body to maximize steady-state power dissipation in the joints of the USR. Simulations show that the system under the ESC scheme autonomously converges to a neighborhood around the optimum that was previously determined through the grid search.

Future work involves experiments to confirm the simulation results on the existence of an optimal distance from the cylinder. Additionally, results from the grid search indicate that the damping coefficients in the joints may also have a significant impact on power dissipation. Thus, employing ESC for joint optimization over distance and damping coefficients will be an interesting avenue of investigation.

ACKNOWLEDGEMENTS

We thank Prof. Mattia Gazzola and Yashraj Bohsale for sharing a preliminary version of the CFD simulator used in this paper, and for fruitful discussions about this. Furthermore, we thank Dr. Caroline Bernier for comments on how the CFD simulator presented in Bernier et al. (2019) can be implemented. Finally, we thank Mark Haring for sharing valuable insight about his work on extremum-seeking control.

REFERENCES

Allen, J.J. and Smits, A.J. (2001). Energy Harvesting Eel. *Journal of Fluids and Structures*, 15(3-4), 629–640.

Ariyur, K.B. and Krstić, M. (2003). *Real-Time Optimization by Extremum-Seeking Control*. John Wiley & Sons, Inc., Hoboken, NJ, USA.

Bernier, C., Gazzola, M., Chatelain, P., and Ronsse, R. (2018). Numerical simulations and development of drafting strategies for robotic swimmers at low reynolds number. In *Proc. IEEE International Conf. Biomedical Robotics and Biomechatronics*. Enschede, The Netherlands.

Bernier, C., Gazzola, M., Ronsse, R., and Chatelain, P. (2019). Simulations of propelling and energy harvesting articulated bodies via vortex particle-mesh methods. *J. of Computational Physics*, 392, 34–55.

Haring, M., van de Wouw, N., and Nešić, D. (2013). Extremum-seeking control for nonlinear systems with periodic steady-state outputs. *Automatica*, 49(6), 1883–1891.

Hazeleger, L., Haring, M., and van de Wouw, N. (2020). Extremum-seeking control for optimization of time-varying steady-state responses of nonlinear systems. *Automatica*, 119, 109068.

Kelasidi, E., Liljebäck, P., Pettersen, K.Y., and Gravdahl, J.T. (2016). Innovation in underwater robots: Biologically inspired swimming snake robots. *IEEE Robotics & Automation Magazine*, 23(1), 44–62.

Krstic, M. and Wang, H.H. (1997). Design and stability analysis of extremum seeking feedback for general nonlinear systems. In *Proc. IEEE Conf. Decision and Control*. San Diego, CA, USA.

Nešić, D., Tan, Y., Moase, W.H., and Manzie, C. (2010). A unifying approach to extremum seeking: Adaptive schemes based on estimation of derivatives. In *Proc. 49th IEEE Conf. Decision and Control*. Atlanta, GA, USA.

Spong, M.W., Hutchinson, S., Vidyasagar, M., et al. (2006). *Robot modeling and control*, volume 3. Wiley New York.